Nanoscale

Morphology dependent near-field response in atomistic plasmonic nanocavities

Journal:	*Nanoscale*
Manuscript ID	NR-ART-04-2018-003029.R1
Article Type:	Paper
Date Submitted by the Author:	16-May-2018
Complete List of Authors:	Chen, Xing; The Pennsylvania State University, Chemistry Jensen, Lasse; The Pennsylvania State University, Chemistry

Journal Name

ARTICLE TYPE

Cite this: DOI: 10.1039/xxxxxxxxxx

Morphology dependent near-field response in atomistic plasmonic nanocavities†

Xing Chen,[a] and Lasse Jensen*[a]

Received Date
Accepted Date

DOI: 10.1039/xxxxxxxxxx

www.rsc.org/journalname

In this work we examine how the atomistic morphologies of plasmonic dimers control the near-field response by using an atomistic electrodynamics model. At large separations, the field enhancement in the junction follows a simple inverse power law as a function of the gap separation, which agrees with classical antenna theory. However, when the separations are smaller than 0.8 nm, the so-called quantum size regime, the field enhancement is screened and thus deviates from the simple power law. Our results show that the threshold distance for the deviation depends on the specific morphology of the junction. The near field in the junction can be localized to an area of less than 1 nm^2 in the presence of an atomically sharp tip, but the separation distances leading to large confinement of near field depend strongly on the specific atomistic configuration. More importantly, the highly confined fields lead to large field gradients particularly in a tip-to-surface junction, which indicates that such plasmonic structure favors observing strong field gradient effects in a near-field spectroscopy. We find that for atomically sharp tips the field gradient becomes significant and depends strongly on the local morphology of a tip. We expect our findings to be crucial for understanding the origin of high-resolution near-field spectroscopy and for manipulating optical cavities through atomic structures in the strongly coupled plasmonic systems.

1 Introduction

One of the defining characteristics of plasmonic systems is the ability to localize light below the diffraction limit. The localized electromagnetic fields in plasmonic junctions at the subwavelength scale have many applications in the fields of enhanced molecular spectroscopy,[1–3] molecular vibrational mapping,[4] and optoelectronics.[5,6] Recent experimental works have demonstrated that the highly confined fields in the junctions can act as sub-nanometric optical cavities enabling single-molecule strong coupling.[7,8] The highly-confined fields lead to sub-nanometric spatial resolution in tip-enhanced Raman scattering,[4,9,10] such that an individual molecule can be imaged[4] and subtle differences between the neighboring molecules can be resolved.[9,10] The extreme confinement of the near field modifies the optical selection rules typically found in far-field spectroscopies.[11]

The prototypical system for understanding the near-field confinement is a plasmonic dimer consisting of two metallic nanoparticles placed nano- or subnano-scale apart.[12–19] Light interacting with strongly coupled nanoparticles localizes the valence electrons across the junction and generates the so-called gap plasmons, which can be drastically modified by the interparticle spacing, curvature, composition, and environment.[20–26] Numerous efforts have been devoted to understanding the gap plasmon behaviors,[13,14,27–29] and the experimental progress has enabled the fabrication of plamonic dimers with subnano-scale separations,[30–32] where the quantum effects are prominent.[33–35] It is known that the bonding dipolar plasmon monotonically redshifts with decreasing plasmonic nanogap.[21,36] The charge-transfer plasmons gradually emerge before physical contact when the induced conductance allows electrons to tunnel across the junction.[21,37] At short distances, the near-field enhancement is suppressed due to tunneling coupling between the two particles.[38–41] It is noted that the far- and near-field properties are sensitive to the morphology of a nanogap.[42–47] Furthermore, the atomic-scale resolution in the plasmonic response is crucial for a deep understanding of the vibrational spectroscopy of single molecule trapped in the nanocavities.[8,48–50]

In this work, we will explore how the near-field localization in plasmonic dimers depends on the atomistic morphology of the junction. To that end, we will use a recently developed atomistic electrodynamics model, namely coordination-dependent discrete interaction model (cd-DIM), which has been shown to provide an efficient description of plasmonics in the quantum-size regime.[50–52] This method represents a nanoparticle as a collec-

Department of Chemistry, The Pennsylvania State University, 104 Chemistry Building, University Park, Pennsylvania 16802, United States. E-mail: jensen@chem.psu.edu

† Electronic Supplementary Information (ESI) available: [additional characterization of far-field and near-field distributions in the junctions]. See DOI: 10.1039/b000000x/

tion of interacting atoms characterized by atomic polarizabilities which are dependent on the local environment with induced dipoles having Gaussian charge distributions. Thus, cd-DIM allows efficient simulations of the near-field localization in nanogaps with dimensions below 1 nm, which otherwise would require a fully quantum mechanical treatment. We find that for large separations ($>$ 0.8 nm) the field enhancement in the gap follows a simple power law. However, for small separations the near field gap dependence deviates from a power law due to the nonlocal screening. Finally, we show that when atomic-like sharp tips are present in the junction near field can be confined to dimensions of few Ångstroms. These extremely confined fields give rise to the large field gradients responsible for the modified selection rules in near-field spectroscopies.[11,50] The quantification of the scaling behavior of near field with sub-nanometric dimensions demonstrated in this work is essential for understanding the high resolutions recently demonstrated in near-field spectroscopies.[4]

2 Methods

cd-DIM represents a nanoparticle as a collection of interacting atoms in terms of dielectric properties that depend on the local chemical environment. Accordingly, surface and bulk atoms can be differentiated. Using a Clausius-Mossotti relation, the atomic polarizability can be written as,

$$\alpha_I = \frac{6}{\pi} R_I^3(X) \frac{\varepsilon(X)-\varepsilon_0}{\varepsilon(X)+2\varepsilon_0}. \quad (1)$$

Atoms are represented by Gaussian charge distributions. $R_I(X)$ is the coordination dependent radius of an atom, $\varepsilon(X)$ is the coordination dependent dielectric constant of the material and ε_0 is the dielectric constant of the environment. The parameterization of $R_I(X)$ and $\varepsilon(X)$ is taken from our previous work.[51] The total polarizability is obtained by minimizing the total energy with respect to the induced atomic dipoles as,

$$\mu_{I,\alpha}^{\text{ind}} = \alpha_{I,\alpha\beta}\left(E_\alpha^{\text{ext}} + \sum_{J\neq I}^{N} T_{IJ,\alpha\beta}^{(2)} \mu_{J,\beta}^{\text{ind}}\right), \quad (2)$$

where $T_{IJ}^{(2)}$ is the second order interaction tensor to describe the interactions between dipole I and J, E_α is the external field and μ_I^{ind} is the induced atomic dipole of atom I. The Einstein summation convention is employed for Greek indexes, which corresponds to the cartesian directions. In cd-DIM, the interaction tensor is renormalized in order to screen the dipole-dipole interactions at short distances.[51,53,54] In the discrete-dipole approximation (DDA) model, the bare unscreened interaction tensor is adopted because the atoms are treated as point charges. Here we ignore retardation effects due to the small size of the nanoparticles, however, the collective response from the interacting dipoles describes locally the higher-order response that are important at short distances. Once these equations have been solved self-consistently the total polarizability is obtained as

$$\alpha_{\alpha\beta}^{\text{NP}} = \sum_{I}^{N} \frac{\partial \mu_{I,\alpha}^{\text{ind}}}{\partial E_\beta^{\text{ext}}}. \quad (3)$$

The near fields around the nanoparticles were obtained directly from the atomic dipoles by using either the renormalized interaction tensor for cd-DIM or the bare interaction tensor for DDA. The near field at a grid point is given by,

$$\mathbf{E}_\alpha = \sum_{I}^{N} T_{\alpha\beta}^{(2)}(\mathbf{R}_I)\mu_{I,\beta}^{\text{ind}} + \delta_{\text{ind},\alpha}, \quad (4)$$

where $\mathbf{R}_I$ is a vector from grid point to atomic dipole I. The near-field gradients were calculated by numerical differentiation between the fields at two adjacent grids along each axis. The magnitude of field gradient is given by,

$$|\nabla \mathbf{E}_z| = \sqrt{\left|\frac{\mathbf{E}_z(x+\Delta x)-\mathbf{E}_z(x-\Delta x)}{2\Delta x}\right|^2 + \left|\frac{\mathbf{E}_z(y+\Delta y)-\mathbf{E}_z(y-\Delta y)}{2\Delta y}\right|^2 + \left|\frac{\mathbf{E}_z(z+\Delta z)-\mathbf{E}_z(z-\Delta z)}{2\Delta z}\right|^2}. \quad (5)$$

For silver nanostructure, the nano-icosahedron and nanocube were built assuming perfect shapes, where the Ag-Ag bond distance is set to 0.2889 nm based on the experimental bond length. Using idealized structures is reasonable as recent work have shown that only small changes to the optical properties arises when optimizing the geometry of the nanoparticles.[43] The monomer structures were fixed when separated in the dimers. Any overlapping atoms were removed as the dimers merge, as shown in Figure 1S.†

3 Results and Discussion

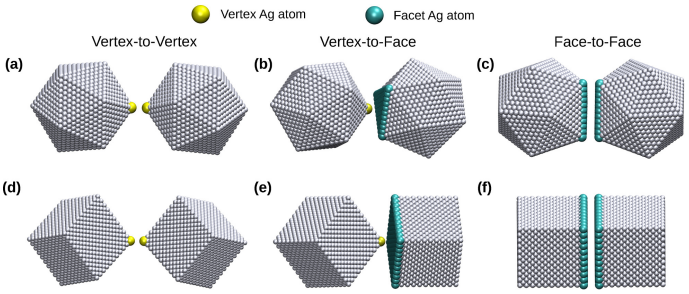

Fig. 1 Atomistic representation of plasmonic dimers in different morphologies. Two nanoparticles are placed to form vertex-to-vertex (a,d), vertex-to-face (b,e), and face-to-face (c,f) configurations. In the plasmonic gap, atoms on the tips are shown in yellow and atoms on the faces in cyan.

To understand how the nanoparticle shape affects the plasmon coupling in the junction we examine two prototypical dimer systems consisting of two interacting icosahedral or two cubic nanoparticles. The length of the nanoparticles was chosen so that they have an equivalent plasmon length of 5.8 nm, which corresponds to 3871 and 4631 silver atoms in the icosahedron and cube, respectively. The plasmon length is defined as the distance between the regions of opposite charge oscillations created by the plasmon.[55] Previously we have shown that for small nanoparticles with identical plasmon lengths the optical response is dominated by the dipolar plasmon so that the far field is essentially shape-independent.[52] In order to explore the effects of symmetric shape and atomic structure of a nanogap, the two nanoparticles are aligned with their geometric centers. The separation (d_{gap}) between two nanoparticles is defined as the shortest dis-

tance between two atoms in the gap. Within physical contact distances between the two nanoparticles ($d_{gap} \leq 0$), we remove some of the overlap atoms as illustrated in supporting information Figure S1.† Three different configurations are considered, vertex-to-vertex, vertex-to-face, and face-to-face. An illustration of the different configurations are shown in Figure 1, where the contact area between the two nanoparticles is highlighted.

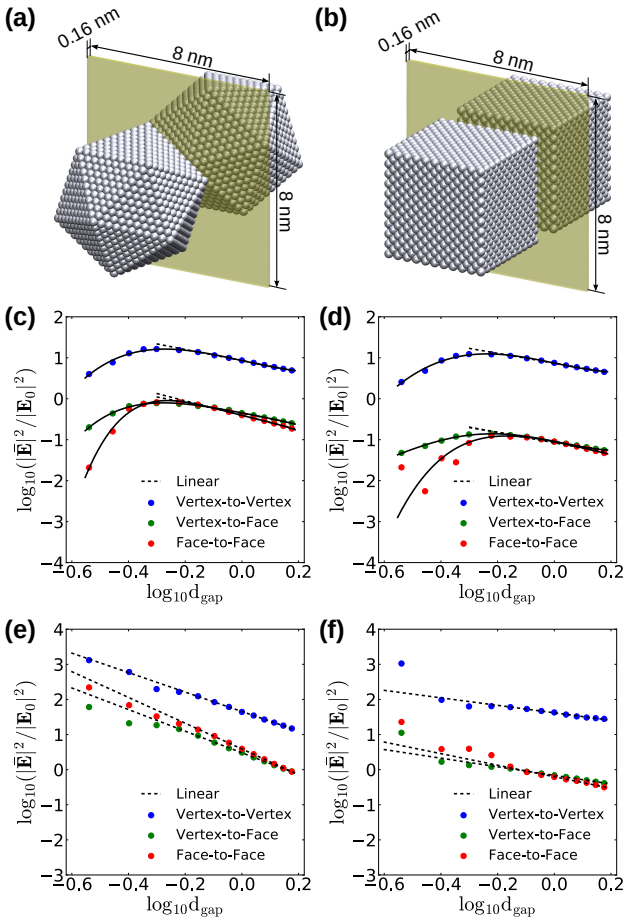

Fig. 2 Average near-field enhancement ($|\bar{\mathbf{E}}|^2/|\mathbf{E}_0|$) as a function of plasmonic separation distance (d_{gap}) on a logarithm scale. The selected volume in the junction schematically shown in (a,b). The blue, green, and red dots represent the results of the vertex-to-vertex, vertex-to-face, and face-to-face configurations of icosahedral (c,e) and cubic dimers (d,f), respectively. Fitting linear functions in dashed lines and quartic polynomial functions in solid lines.

The far-field responses of the nanoparticle dimers are strongly morphology-dependent, compared to the optical properties of the individual nanoparticles, as shown in Figure S2 of the supporting information. We find that the low-energy charge-transfer plasmon prominently blue shifts as the contact area increases. Overall, we find good agreement with previous results as discussed in the supporting information. The main plasmon mode varies with separation distance as illustrated in Figure S3 of the supporting information. The difference in the optical properties is likely ascribed to the morphology-dependent interactions between nanoparticles, which may also impact the near-field response in strongly coupled nanoparticles. Previous work has demonstrated that the near-field enhancement as a function of gap separation follows a simple power law as $\frac{|\mathbf{E}|^2}{|\mathbf{E}_0|^2} \propto d_{\text{gap}}^{-k}$.[56] In this work it was shown that the exponent for nanostructure was less than two predicted from classical antenna theory.[56] To explore how this scaling behavior is modified by the morphology of the junction in the quantum size regime, we plot the distance-dependent average near field in Figure 2. To enable a direct comparison between cubic and icosahedral nanoparticles, we define the average near field in the junction as,

$$|\bar{\mathbf{E}}| = \frac{\sum_{i=1}^{N} |\mathbf{E}_i(x,y,z)|}{N_{\text{grid}} N_{\text{atom}}}, \tag{6}$$

where $|\mathbf{E}(x,y,z)|$ is the modulus of the induced near field in a volume centered at the junction. The number of grids points, N_{grid}, is 8405 evenly distributed in a volume of $8 \times 8 \times 0.16$ nm, which is schematically represented in Figure 2a and b. N_{atom} reflects the size of the contact area in the junction and depends on the specific morphology of the gap. For the icosahedral dimers, N_{atom} is 2, 55, 112 for the vertex-to-vertex, vertex-to-face, and face-to-face configurations, respectively, whereas for the cubic dimers, N_{atom} is 2, 222, 442, respectively. Accordingly, the average near field represents the contribution per atom within the contact area. In all simulations the incident field is polarized along the dimer axis assuming an incident frequency that leads to the maximal field in the center of a gap. For large separations, this frequency is roughly equivalent to the bonding dipolar plasmon. However, at short separations, the frequency redshifts as shown in Figure S2.† We show the comparison of the near-field enhancement between cd-DIM (in Figure 2 c and d) and the DDA variant, which assumes point dipoles rather than the Gaussian charge distributions (in Figure 2 e and f). Both cd-DIM and DDA use the same atomic structures of the nanoparticle dimers, and thus, the comparison between these two models allows us to understand how the scaling law is impacted by the screening of near field in the junction.

For the gap distances larger than 0.8 nm, we see the average field enhancement follows a simple power law. The exponents for the different dimers are collected in Table 1. In general, the exponents are larger in the icosahedral dimers than in the cubic dimers. Also, larger exponents are found in DDA than in cd-DIM except for the cubic dimer in the vertex-to-vertex configuration. The screened dipoles used in the cd-DIM model lead to a reduction in the near-field coupling between the two nanoparticles and thus lowers the exponents. Using DDA we find for the icosahedral dimers that the exponents are larger than those found previously for large nanostructures and that expected from classical antenna theory.[56] One possible reason is that previous work had considered significantly larger nanostructures, where retardation effects are important. Thus, to examine if the size of nanoparticles influences the near-field scaling we simulated the gap dependence of two interacting spherical nanoparticles using the generalized nonlocal optical response model (GNOR).[57] The results are shown in Figure S5† for nanoparticles with radii ranging from 1 to 60 nm, and illustrate that the scaling exponent depends strongly on the size. The simulations show that the scaling exponent becomes larger for smaller particles which is in agreement with the

DDA simulations. This may be caused by the additional radiative losses for large particles thus hindering the localization of near fields. In the quantum size regime the smeared-out charge-distributions also lead to a reduction in the scaling exponent.

Table 1 Parameters, threshold distance, d_{thd}(in nm) and slope k, determining the distance dependence of the near-field enhancement.

Nanoparticle	Vertex-to-Vertex	Vertex-to-Face	Face-to-Face
Icosahedron			
d_{thd}	0.54	0.53	0.55
$k_{\mathrm{cd-DIM}}$	1.36	1.32	1.77
k_{DDA}	2.78	3.08	3.67
Cube			
d_{thd}	0.58	0.60	0.68
$k_{\mathrm{cd-DIM}}$	1.20	1.16	1.27
k_{DDA}	1.07	1.23	1.65

In general, when the separation becomes less than 0.8 nm the near-field enhancements begin to deviate from the simple power law due to the screening effects. However, DDA predicts a significant increase in the near-field enhancement even at short gap distances as a result of the well-known shortcomings of classical electrodynamics.[35,42,43,46] In contrast, cd-DIM captures the decrease of the near-field enhancement at short distances as the model considers the smeared-out charge distribution in the junction.[51] The deviation from a simple power law at short distances allows us to identify a threshold distance, denoted by d_{thd}, which is a turnover point indicating the onset of the near-field screening. Importantly, it provides a quantitative description on how the atomistic morphology impacts the near-field screening in order to make a comparison between the different morphologies. In Table 1 the threshold distances for the different configurations are listed. We find that d_{thd} is stable at 0.54 ± 0.01 nm for the icosahedral dimers, but d_{thd} changes from 0.58 to 0.73 nm in the cubic dimers and thus, depends strongly on the junction morphology. The face-to-face cubic dimer can be considered as two parallel nano-plates similar to a flat capacitor junction with a smeared charge distribution across the gap even at relatively longer distances. The presence of a vertex in the junction mainly reduces the contact area. As a result, the electron screening occurs at relatively shorter distances, as shown in the vertex-to-vertex and vertex-to-face configurations. The threshold distances found in this work are consistent with ∼0.5 nm reported in a previous work.[35]

The nanometer resolution recently demonstrated in a TERS experiment[4] indicates the importance of the highly confined near field. Theoretical simulations have demonstrated that the high localization of near field arises from atomic-scale structure of a junction.[11,43,50,58] Here we quantify the near-field localization as a function of gap distance for the different morphologies. The localization area of near field in a junction is calculated as,

$$S_{\mathrm{field}} = \frac{1}{h}\sum_{i=1}^{N}\frac{|\mathbf{E}_i(x,y,z)|^2}{|\mathbf{E}_{\mathrm{max}}|^2}\frac{V}{N_{\mathrm{grid}}}, \qquad (7)$$

where V is the volume with dimensions of $8 \times 8 \times 0.16$ nm^3 in the junction center and h is the thickness. $|\mathbf{E}_{\mathrm{max}}|$ is the maximal field in the gap region. A comparison of the near-field localization obtained from DDA and cd-DIM is shown in Figure 3. Overall, cd-DIM predicts that the near fields become more localized as the gap distance decreases until the charge-transfer plasmon is established. A three-dimensional representation of the near-field localization is shown in the supporting information (Figure S6 and S7). As the separation reaches the threshold distance we see that the near fields are slowly expelled from the junction with increasing delocalization as the distance decreases further. As expected the localization depends on the size of the contact area, the near fields are less localized in the face-to-face configuration and highly confined in the vertex-to-vertex configuration. Overall, we see that the near fields can be confined to an area less than 1 nm^2 for junctions with atomically sharp tips. Not surprisingly, the DDA results show that the fields can effectively be localized to a single point irrespective of the atomic configuration (Figure 3e and f.) The field delocalization at short distances are absent since DDA neglects the smearing of the charge distribution, which becomes more critical at small gap separations. These results are consistent with results obtained from TDDFT and shows that below ∼ 1 nm the classical result cannot predict the field localization.[58] The results obtained here are also in good agreement with the recent results using finite element methods using an atomic protrusion model.[59]

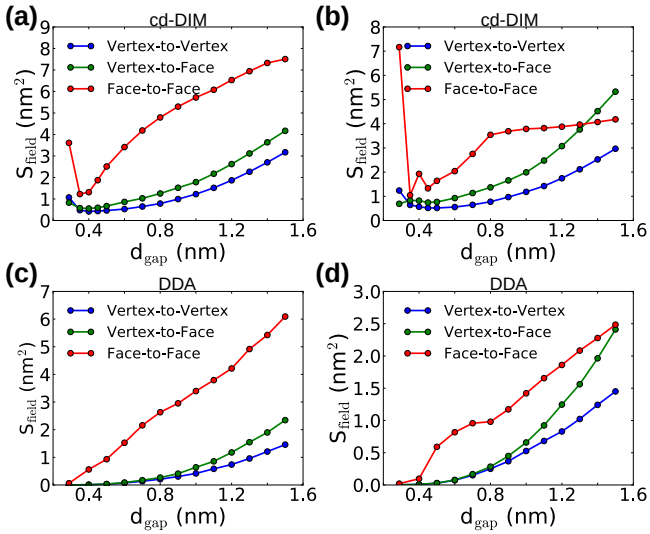

Fig. 3 The near-field localization (S_{field}) as a function of gap distance (d_{gap}). The blue, green, and red curves are results of the vertex-to-vertex, vertex-to-face, and face-to-face configurations of icosahedral (a,c) and cubic dimers (b,d), respectively. For the face-to-face configuration of the cubic dimer, the plot is multiplied by 0.2 so that it can be plotted together with the other configurations.The incident field is polarized along the dimer axis with the near fields aligned with the dimer-axis.

The fact that the near field can be localized to sub-nanometric dimensions implies that the fields vary over of the length of typical molecules and thus field-gradient effects should be important and observable in the high-resolution TERS experiments. Indeed recent simulations and experiments have demonstrated that field gradients play a prominent role in high-resolution TERS and particularly determine the observed Raman spectra.[11,50] The field-gradient effects modify the traditional dipole surface selection

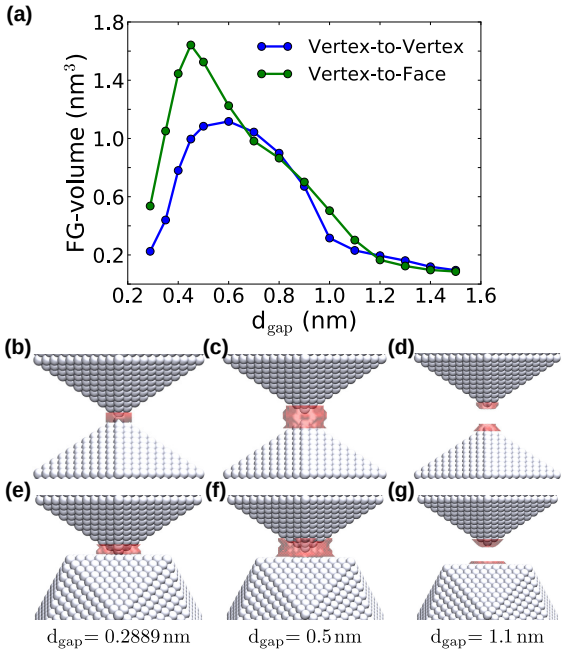

Fig. 4 The FG-volume of the ratio of field and field gradient less than 0.6 nm for vertex-to-vertex and vertex-to-face icosahedral dimers as a function of plasmonic gap distance (d$_{gap}$) (a). The blue and green curves correspond to the results for the vertex-to-vertex and vertex-to-face configurations, respectively. The FG-volume distributions in vertex-to-vertex (top panel) and vertex-to-face (bottom panel) junctions with an isovalue of 0.6 nm at the selected separation distances of 1.1 (b,e), 0.5 (c,f), and 0.2889 nm (d,g), respectively.

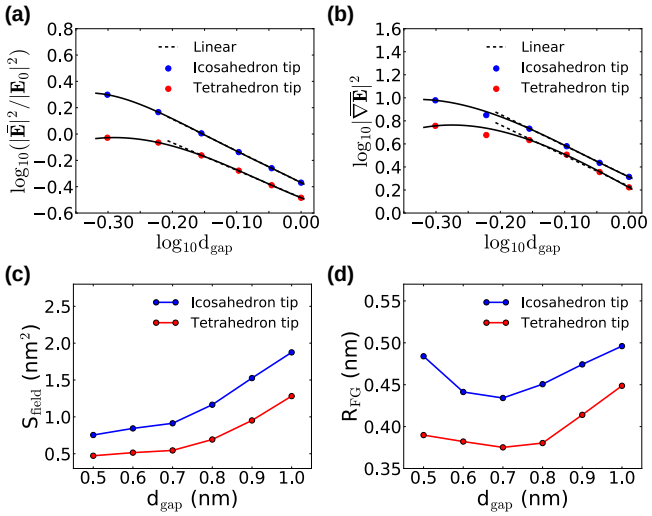

Fig. 5 Distance dependence of the near-field, field gradient, and ratio of field and field gradient in tip-to-surface plasmonic structures. The average field (a) and field gradient (in nm^{-1})(b) enhancement as a function of gap distance (in nm) on a logarithm scale. The near-field localization (in nm^2) (c) and average ratio (in nm) (d) as a function of gap distance. The average field and field gradient calculated in a junction where the volume in the shape of cylinder with the radius of 1.5 nm and the thickness of 0.12 nm centered at 0.3 nm above a substrate. The incident field polarized along the z-axis (tip direction).

rules known from far-field spectroscopy.[4,11] The importance of field-gradient effects is largely determined by the $|\mathbf{E}|/|\nabla\mathbf{E}|$ ratio (FG Ratio) which gives a measure on the length-scale over which the near fields vary.[60,61] If this ratio is small compared to the dimensions of a molecule in the junction and the fields are large then the field-gradient effects are likely to be important. To understand how the field-gradient effects depend on the junction morphology we compare the ratio for the vertex-to-vertex and vertex-to-face configurations of the icosahedral dimer. In Figure 4a we plot the field-gradient volume (FG-volume) where the FG ratio is smaller than 0.6 nm as a function of gap separation for the two configurations. The larger FG-volume indicates more prominent field-gradient effects, and thus it is more likely that a molecule can be found within the volume. We see that the FG-volume grows as the distance decreases until around 0.6 nm for the vertex-to-vertex configuration and 0.5 nm for the face-to-vertex configuration. The decrease of the FG-volume at shorter distances is likely due to the screening of near field in the junction, which reduces both fields and field gradients. We also see that for small separations the FG-volume becomes larger in the vertex-to-face configuration even though the near field is more localized in the vertex-to-vertex dimer. To visualize the FG-volume changes as the gap distance decreases, we plot the FG-volume distributions at selected separations of 1.0, 0.5, and 0.2889 nm in Figure 4 b-g, respectively. The near field, field gradient, and ratio distributions at different gap distances are presented in Figure S8 and S9.† Although the vertex-to-vertex and vertex-to-face configurations has the same FG-volume, the field gradients are localized on the atomically sharp tips and thus shows different distributions. For the vertex-to-face configuration at a distance of 0.6 nm, the contact area between the tip and the face leads to a larger FG-volume. Therefore, one can expect that the field-gradient effects are more prominent in tip-to-surface junction. This structure used in high-resolution TERS or the nanoparticle-on-a-film configurations might be more favorable for observing strong field-gradient effects in near-field spectroscopy.

Therefore, to further explore how the local morphology affects the near field and field gradient we examine two typical atomistic tips, icosahedron and tetrahedron, as placed on a flat substrate. The substrate surface is orientated on the xy-plane and the tip is perpendicular to the flat surface in dimensions of 7.5 $\times$ 7.5 nm. Assuming a typical distance ($\sim$ 0.3 nm) between adsorbed molecules and metal surface, we chose to quantify the average near field and field gradient in a cylinder with a radius of 1.5 nm and a thickness of 0.12 nm centered at 0.3 nm above the substrate. The correlation between the average field/ field gradient and gap distance on a logarithm scale is plotted in Figure 5a and b. We see that both the average field and field gradient follow a simple inverse power law at long separation distances, as shown by the dashed black lines in Figure 5a and b. At short distances both the field and field gradient deviate from the power law due to the smearing of field. The turn-over point for both field and field gradient are similar since the near-field smearing reduces the local variation of the fields.

We further explored the tip curvature effects on the distance-dependent near-field localization (S_{field}) and the average FG ratio.

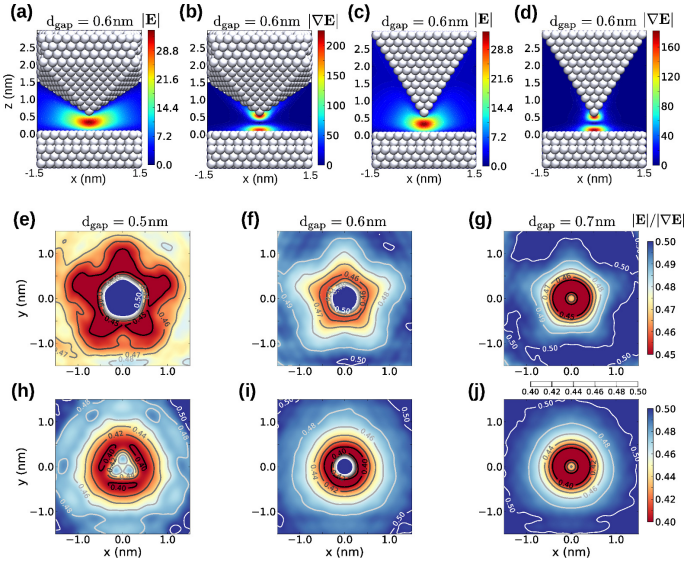

Fig. 6 Near-field, field-gradient, and FG ratio distribution. The near-field (a,c) and field-gradient (b,d) distributions on the xz-planes through the atomic tips. The FG ratio distributions on the xy-plane at 0.3 nm above the substrate with separations of 0.5 (e, h), 0.6 (f, i), and 0.7 (g, j) nm, respectively. The distributions in the icosahedral junction (top panel) and tetrahedral junction (bottom panel) junctions. The incident field is polarized along the tip axis at the frequencies inducing the maximal field in the scanning plane.

The near-field localization area was calculated according to Equation 7. The field gradient effects in the effective localization area can be quantified through the average FG ratio, which is written as,

$$R_{\mathrm{FG}} = \frac{1}{N_{\mathrm{grid}}} \sum_{i}^{S_{\mathrm{field}} \not\supset S_{\mathrm{tip}}} \frac{|\mathbf{E}_i(x,y,z)|}{|\nabla \mathbf{E}_i(x,y,z)|}. \quad (8)$$

It should be noted that in the effective localization area we exclude the area nearest to the tip, S_{tip}, where the field gradients are very small (see Figure S10).† Overall, we see that the near fields are more localized in the tetrahedral junction. The near-field localizes below 1 nm^2 at a distance of ~ 0.9 nm for the tetrahedral junction whereas this occurs at a distance of ~ 0.7 nm for the icosahedral junction. Thus, the higher curvature of the tetrahedral junction as compared to the icosahedral junction leads to a more effective localization of the near field. Interestingly, we find that the average FG ratios are less than 0.5 nm in both tips, indicating the field-gradient magnitude is significant within the confined area (see Figure 5d). More importantly, we find that the average FG ratio increases at short distances even though the field localization remains constant. The higher curvature of the tetrahedral junction leads to the smaller average FG ratio at all distances and not just at short distances. Thus, an atomically terminated tip with a high curvature is more likely to offer highly confined near fields with prominent field-gradient effects. Therefore, a break down of the traditional selection rule in near-field spectroscopy is expected under these conditions.

To visualize the near fields and field gradients in the junctions, we plot the near-field and field-gradient distributions on the xz-plane in Figure 6 (a-d) for a gap distance of 0.6 nm. From the figure we see that the near fields are confined in the junctions with the most intense fields at 0.3 nm above the substrate. Furthermore, the near fields are more localized by the tetrahedral tip than by the icosahedral tip due to the larger curvature. We find that in general the near-field distributions can be reasonably described by Gaussian distributions (see Figure S10, S11, and S12)†, although with very different out-of-plane vs. in-plane distributions. Gaussian field distribution is often used in simulating high-resolution images[4,8,62,63] and it seems to be reasonable as long as the in-plane and out-of-plane distributions are treated differently. Compared to the near fields, the most intense field gradients appear at the atomically sharp tips and flat substrate. The field gradients are near to zero in the center of the junction, where the field is maximal.

The FG ratio distributions on the xy-plane at 0.3 nm above the substrate are illustrated in Figure 6(e-g and h-j), which provides information about how the field-gradient effects vary in the scanning plane of a high-resolution TERS experiment. We see as the separation decreases from 0.7 to 0.5 nm, the central area characterized with large FG ratio increases. At the same time, the near fields become more localized, which explains why the average FG ratio increases as the distance decreases(Figure 5 d). For smaller separation, we also note that the FG ratio distribution reflects the local morphology of a tip. One can expect that for a molecule in the vicinity of a tip experiences both strong field and fields gradients and thus, different tips may lead to different single molecular images when the tip is close enough to the molecule. As demonstrated here, the highly confined fields lead to strong field gradient effects that can modify the traditional selection rules. For example, in traditional SERS the enhancement is determined by the transition polarizability of the molecule and scales as $|\mathbf{E}_{\mathrm{loc}}|^4$. However, if the field gradients are stronger than the fields as demonstrated here, the Raman scattered light is dominated by the electric quadrupole-quadrupole transition polarizability with an enhancement that scales as $|\nabla \mathbf{E}_{\mathrm{loc}}|^4$.[61] Under these conditions, the surface selection rules drastically change and the Raman spectrum might exhibit distinct features compared to the traditional far-field spectrum. A recent experimental and theoretical study of the Raman scattering of Co(II)-Tetraphenylporphyrin on Au(111) supports this.[11]

4 Conclusions

In this work we have systematically investigated the dependence of the plasmonic response on the atomistic morphology of nanoparticle dimers. For large separations the field enhancement localized in the junction follows a simple inverse power law as a function of the gap separation in consistence with classical antenna theory. However, for gap distance in the quantum size regime, the field enhancement is suppressed leading to deviation from the simple power law that depends strongly on the specific morphology of the junction. We show that the near field can be highly localized to an area of less than 1 nm^2 for junction with an atomically sharp tip. Furthermore, we demonstrate that for these highly confined fields the field gradient effects are significant. Our simulations shows that the field-gradient distribution is sensitive to the local morphology of the junction and depends

strongly on the tip curvature. This work shows that one should expect different surface-selection rules in high-resolution near-field spectroscopies due to the highly confined field with large field gradients. Our findings provide insight into understanding the field and field-gradient effects on high-resolution near-field spectroscopy which is helpful to the development of optical cavities created by strongly coupled plasmonic systems and sub-nanometric probes.

Conflicts of interest

There are no conflicts to declare.

Acknowledgements

X.C. and L.J. acknowledge the support from the National Science Foundation Center for Chemical Innovation dedicated to Chemistry at the Space-Time Limit (CaSTL) Grant CHE-1414466. Portions of this work were conducted with Advanced CyberInfrastructure computational resources provided by The Institute for CyberScience at The Pennsylvania State University (`http://ics.psu.edu`).

Notes and references

1 K. A. Willets and R. P. Van Duyne, *Ann. Rev. Phys. Chem.*, 2007, **58**, 267–297.
2 H. Xu, E. J. Bjerneld, M. Käll and L. Börjesson, *Phys. Rev. Lett.*, 1999, **83**, 4357–4360.
3 H. Xu, J. Aizpurua, M. Käll and P. Apell, *Phys. Rev. E*, 2000, **62**, 4318–4324.
4 R. Zhang, Y. Zhang, Z. C. Dong, S. Jiang, C. Zhang, L. G. Chen, L. Zhang, Y. Liao, J. Aizpurua, Y. Luo, J. L. Yang and J. G. Hou, *Nature*, 2013, **498**, 82–86.
5 J. C. Prangsma, J. Kern, A. G. Knapp, S. Grossmann, M. Emmerling, M. Kamp and B. Hecht, *Nano Lett.*, 2012, **12**, 3915–3919.
6 A. Demming, M. Brongersma and D. S. Kim, *Nanotechnology*, 2012, **23**, 440201.
7 R. Chikkaraddy, B. de Nijs, F. Benz, S. J. Barrow, O. A. Scherman, E. Rosta, A. Demetriadou, P. Fox, O. Hess and J. J. Baumberg, *Nature*, 2016, **535**, 127.
8 F. Benz, M. K. Schmidt, A. Dreismann, R. Chikkaraddy, Y. Zhang, A. Demetriadou, C. Carnegie, H. Ohadi, B. de Nijs, R. Esteban, J. Aizpurua and J. J. Baumberg, *Science*, 2016, **354**, 726–729.
9 S. Jiang, Y. Zhang, R. Zhang, C. Hu, M. Liao, Y. Luo, J. Yang, Z. Dong and J. G. Hou, *Nat. Nanotechnol.*, 2015, **10**, 865.
10 N. Chiang, X. Chen, G. Goubert, D. V. Chulhai, X. Chen, E. A. Pozzi, N. Jiang, M. C. Hersam, T. Seideman, L. Jensen and R. P. Van Duyne, *Nano Lett.*, 2016, **16**, 7774–7778.
11 J. Lee, N. Tallarida, X. Chen, P. Liu, L. Jensen and V. A. Apkarian, *ACS Nano*, 2017, **11**, 11466–11474.
12 D. R. Ward, F. Huser, F. Pauly, J. C. Cuevas and D. Natelson, *Nat. Nanotechnol.*, 2010, **5**, 732–736.
13 K.-H. Su, Q.-H. Wei, X. Zhang, J. J. Mock, D. R. Smith and S. Schultz, *Nano Lett.*, 2003, **3**, 1087–1090.
14 T. Atay, J.-H. Song and A. V. Nurmikko, *Nano Lett.*, 2004, **4**, 1627.
15 P. Nordlander, C. Oubre, E. Prodan, K. Li and M. I. Stockman, *Nano Lett.*, 2004, **4**, 899.
16 P. Nordlander and E. Prodan, *Nano Lett.*, 2004, **4**, 2209–2213.
17 S. K. Ghosh and T. Pal, *Chem. Rev.*, 2007, **107**, 4797–4862.
18 G. Haran, *Acc. Chem. Res.*, 2010, **43**, 1135–1143.
19 L. Du, D. Y. Lei, G. Yuan, H. Fang, X. Zhang, Q. Wang, D. Tang, C. Min, S. A. Maier and X. Yuan, *Sci. Rep.*, **3**, 3064.
20 E. Hao and G. C. Schatz, *J. Chem. Phys.*, 2004, **120**, 357–366.
21 I. Romero, J. Aizpurua, G. W. Bryant and F. J. García De Abajo, *Opt. Express*, 2006, **14**, 9988.
22 F. Chen, N. Alemu and R. L. Johnston, *AIP Adv.*, 2011, **1**, 032134.
23 O. Pérez-González, N. Zabala and J. Aizpurua, *New J. Phys.*, 2011, **13**, 083013.
24 Y. Wang, Z. Li, K. Zhao, A. Sobhani, X. Zhu, Z. Fang and N. J. Halas, *Nanoscale*, 2013, **5**, 9897–9901.
25 S. Linic, U. Aslam, C. Boerigter and M. Morabito, *Nat. Mater.*, 2015, **14**, 567–576.
26 D. Knebl, A. Hörl, A. Trügler, J. Kern, J. R. Krenn, P. Puschnig and U. Hohenester, *Phys. Rev. B*, 2016, **93**, 081405.
27 J. Zuloaga, E. Prodan and P. Nordlander, *Nano Lett.*, 2009, **9**, 887.
28 K. J. Savage, M. M. Hawkeye, R. Esteban, A. G. Borisov, J. Aizpurua and J. J. Baumberg, *Nature*, 2012, **491**, 574–577.
29 D. C. Marinica, M. Zapata, P. Nordlander, A. K. Kazansky, P. M. Echenique, J. Aizpurua and A. G. Borisov, *Sci. Adv.*, 2015, **1**, e1501095.
30 B. Gao, G. Arya and A. R. Tao, *Nature Nanotechnology*, 2012, **7**, 433–437.
31 C. Ciracì, R. T. Hill, J. J. Mock, Y. Urzhumov, A. I. Fernández-Domnguez, S. A. Maier, J. B. Pendry, A. Chilkoti and D. R. Smith, *Science*, 2012, **337**, 1072–1074.
32 S. F. Tan, L. Wu, J. K. W. Yang, P. Bai, M. Bosman and C. A. Nijhuis, *Science*, 2014, **343**, 1496–1499.
33 F. J. García de Abajo, *J. Phys. Chem. C*, 2008, **112**, 17983.
34 V. Kulkarni and A. Manjavacas, *ACS Photonics*, 2015, **2**, 987–992.
35 W. Zhu, R. Esteban, A. G. Borisov, J. J. Baumberg, P. Nordlander, H. J. Lezec, J. Aizpurua and K. B. Crozier, *Nat Commun.*, 2016, **7**, 11495.
36 D. Marinica, A. Kazansky, P. Nordlander, J. Aizpurua and A. G. Borisov, *Nano Lett.*, 2012, **12**, 1333–1339.
37 J. A. Scholl, A. García-Etxarri, A. L. Koh and J. A. Dionne, *Nano Lett.*, 2013, **13**, 564–569.
38 M. Danckwerts and L. Novotny, *Phys. Rev. Lett.*, 2007, **98**, 026104.
39 W. Zhu and K. B. Crozier, *Nat Commun.*, 2014, **5**, 5228.
40 V. Kravtsov, S. Berweger, J. M. Atkin and M. B. Raschke, *Nano Lett.*, 2014, **14**, 5270–5275.
41 G. Hajisalem, M. S. Nezami and R. Gordon, *Nano Lett.*, 2014, **14**, 6651–6654.
42 P. Zhang, J. Feist, A. Rubio, P. García-González and F. J.

García-Vidal, *Phys. Rev. B*, 2014, **90**, 161407.
43 M. Barbry, P. Koval, F. Marchesin, R. Esteban, A. G. Borisov, J. Aizpurua and D. Sánchez-Portal, *Nano Lett.*, 2015, **15**, 3410–3419.
44 R. Esteban, G. Aguirregabiria, A. G. Borisov, Y. M. Wang, P. Nordlander, G. W. Bryant and J. Aizpurua, *ACS Photonics*, 2015, **2**, 295–305.
45 T. P. Rossi, A. Zugarramurdi, M. J. Puska and R. M. Nieminen, *Phys. Rev. Lett.*, 2015, **115**, 236804.
46 A. Varas, P. GarcÃ■a-GonzÃąlez, F. J. GarcÃ■a-Vidal and A. Rubio, *J. Phys. Chem. Lett.*, 2015, **6**, 1891–1898.
47 D. Lee and S. Yoon, *J. Phys. Chem. C*, 2016, **120**, 20642–20650.
48 J.-M. Nam, J.-W. Oh, H. Lee and Y. D. Suh, *Acc. Chem. Res.*, 2016, **49**, 2746–2755.
49 A. B. Zrimsek, N. Chiang, M. Mattei, S. Zaleski, M. O. McAnally, C. T. Chapman, A.-I. Henry, G. C. Schatz and R. P. Van Duyne, *Chem. Rev.*, 2016, **117**, 7583–7613.
50 P. Liu, D. V. Chulhai and L. Jensen, *ACS Nano*, 2017, **11**, 5094–5102.
51 X. Chen, J. Moore, M. Zekarias and L. Jensen, *Nat Commun.*, 2015, **6**, 8921.
52 X. Chen and L. Jensen, *J. Opt.*, 2016, **18**, 074009.
53 A. Mayer, *Phys. Rev. B*, 2007, **75**, 045407.
54 L. L. Jensen and L. Jensen, *J. Phys. Chem. C*, 2009, **113**, 15182–15190.
55 E. Ringe, M. R. Langille, K. Sohn, J. Zhang, J. Huang, C. A. Mirkin, R. P. V. Duyne and L. D. Marks, *J. Phys. Chem. Lett.*, 2012, **3**, 1479–1483.
56 J. M. McMahon, S. K. Gray and G. C. Schatz, *Phys. Rev. B*, 2011, **83**, 115428.
57 N. A. Mortensen, S. Raza, M. Wubs, T. Søndergaard and S. I. Bozhevolnyi, *Nat Commun.*, 2014, **5**, 3809.
58 M. Urbieta, M. Barbry, Y. Zhang, P. Koval, D. SÃąnchez-Portal, N. Zabala and J. Aizpurua, *ACS Nano*, 2018, **12**, 585–595.
59 S. Trautmann, J. Aizpurua, I. Gotz, A. Undisz, J. Dellith, H. Schneidewind, M. Rettenmayr and V. Deckert, *Nanoscale*, 2017, **9**, 391–401.
60 C. M. Aikens, L. R. Madison and G. C. Schatz, *Nat. Photonics*, 2013, **7**, 508–510.
61 D. V. Chulhai and L. Jensen, *J. Phys. Chem. C*, 2013, **117**, 19622–19631.
62 S. Duan, G. Tian, Y. Ji, J. Shao, Z. Dong and Y. Luo, *J. Am. Chem. Soc.*, 2015, **137**, 9515–9518.
63 S. Duan, G. Tian and Y. Luo, *Angew. Chem., Int. Edit.*, 2016, **55**, 1041–1045.

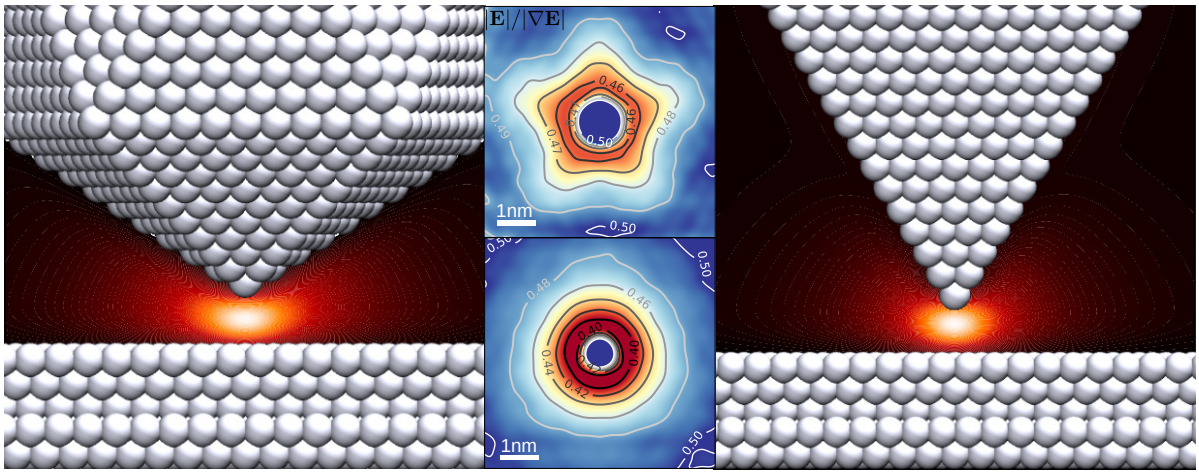

We show the importance of field-gradient effects in plasmonic nanocavities.